Provided for non-commercial research and education use.
Not for reproduction, distribution or commercial use.

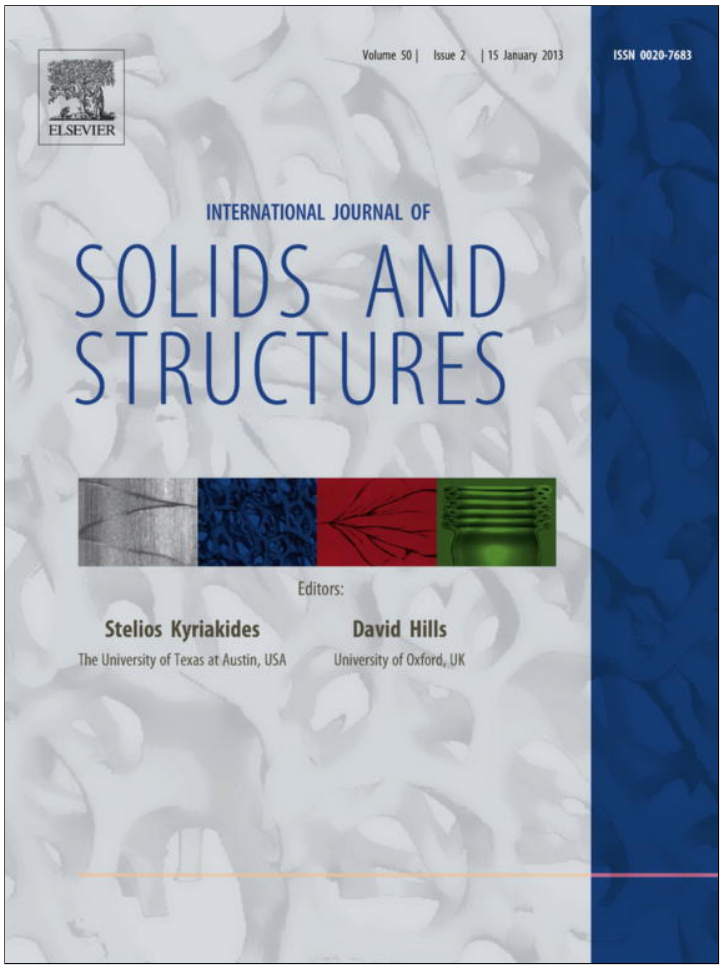

This article appeared in a journal published by Elsevier. The attached copy is furnished to the author for internal non-commercial research and education use, including for instruction at the authors institution and sharing with colleagues.

Other uses, including reproduction and distribution, or selling or licensing copies, or posting to personal, institutional or third party websites are prohibited.

In most cases authors are permitted to post their version of the article (e.g. in Word or Tex form) to their personal website or institutional repository. Authors requiring further information regarding Elsevier's archiving and manuscript policies are encouraged to visit:

http://www.elsevier.com/copyright

Author's personal copy

International Journal of Solids and Structures 50 (2013) 279–287

Contents lists available at SciVerse ScienceDirect

International Journal of Solids and Structures

journal homepage: www.elsevier.com/locate/ijsolstr

Onset of failure in a fiber reinforced elastomer under constrained bending

E. Lignon [a], P. Le Tallec [b], N. Triantafyllidis [b,c,*]

[a] MFP Michelin, 63040 Clermont-Ferrand Cedex, France
[b] Laboratoire de Mécanique des Solides, C.N.R.S. UMR7649 & Département de Mécanique, École Polytechnique, ParisTech, 91128 Palaiseau Cedex, France
[c] Aerospace Engineering Department & Mechanical Engineering Department The University of Michigan, Ann Arbor, MI 48109-2140, USA

ARTICLE INFO

Article history:
Received 27 March 2012
Received in revised form 24 July 2012
Available online 25 September 2012

Keywords:
Fiber-reinforced composite materials
Stability analysis
In-plane buckling
Hyperelasticity
Finite strains

ABSTRACT

Fiber reinforced elastomers subjected to compressive loads are prone to failure initiated by fiber buckling, a phenomenon of great technological importance. A 2*D* bifurcation analysis for an infinite ply-reinforced elastomer, subjected to constrained bending, is hereby presented for determining the composite's critical (i.e. lowest) curvature and associated eigenmode. The study is complemented by a full 3*D* analysis of the same composite.

More specifically, the onset of bifurcation analysis is based on the Bloch wave representation of the 3*D* eigenmode and the periodic, over a 2*D* unit cell, principal solution of the infinite, perfect composite subjected to constrained (i.e. its top layer is bonded to an inextensible metallic plate) bending. The critical curvature and corresponding eigenmode are found by minimizing the lowest bifurcation curvature as a function of the eigenmode's wavelengths. These semi-analytical results, based on a 2*D* Finite Element Method (F.E.M) representation of the unit cell, are found to be in remarkable agreement with the full 3*D* calculations of the corresponding imperfect composite, thus establishing the usefulness of the proposed analysis. A comparison of the numerical simulation results to some limited experimental data is also discussed.

© 2012 Elsevier Ltd. All rights reserved.

1. Introduction and motivation

Fiber-reinforced polymer matrix composites are widely used in engineering applications because of their high axial stiffness and strength-to-weight ratios, when compared to conventional structural materials. In contrast to their tensile strength, their resistance to compressive loads is considerably diminished due to fiber buckling. There is an impressive amount of engineering literature dealing with this subject, the review of which is beyond the scope of this paper.

The work at hand pertains to the special case of fiber-reinforced elastomer-matrix composites subjected to constrained bending, a test of interest to the tire industry (see (Orjela et al., 1998; Schaffers, 1977; Astier and Caillard, 2006)), since it allows the study of certain tire failure mechanisms. A related application of technological interest involves composite spring hinges (see (Lopez Jiménez and Pellegrino, 2012) and references quoted therein), since compressive axial stresses on the fibers are responsible for a buckling instability in a plane perpendicular to the plane of bending, a feature that allows for the imposition of high curvatures in fiber-reinforced composites without breaking the fibers (a stable post-bifurcation exists, in contrast to the in-plane compression of composites that results in kinking). Motivated by the experiments of Astier and Caillard (2006), a 2*D* bifurcation analysis for a perfect, infinite ply-reinforced elastomer, subjected to constrained bending, is hereby presented for determining the composite's critical (i.e. lowest) curvature and associated eigenmode, complemented by a full 3*D* analysis of the same composite.

The composite at hand has a regular microstructure with a periodic unit cell. For such cases, and under the additional assumption of the existence of an energy density (i.e. hyperelastic solids), the work of Muller (1987) has shown that although a homogenized energy density function theoretically exists, it is not rank-one convex and, more importantly, it cannot be explicitly determined. The reason of this difficulty is the development of microstructural buckling in these solids, in patterns that involve an arbitrary number of unit cells. A connection was discovered between local, also termed "*microscopic*", instabilities (microscopic buckling in patterns that repeat over a finite number of unit cells) and the corresponding global, also termed "*macroscopic*" ones, (buckling pattern involves an infinite number of unit cells) by Triantafyllidis and Maker (1985) for an infinite, incompressible, hyperelastic layered composite under plane-strain. Subsequent work by Geymonat et al. (1993) established a rigorous connection between the onset of bifurcation instability and loss of rank-one convexity of the homogenized moduli in finitely strained periodic hyperelastic solids of infinite extent. A key idea in this work, which allows one to

* Corresponding author at: Aerospace Engineering Department & Mechanical Engineering Department The University of Michigan, Ann Arbor, MI 48109-2140, USA. Tel.: +1 734 763 2356; fax: +1 734 763 0578.
E-mail address: nick@lms.polytechnique.fr (N. Triantafyllidis).

0020-7683/$ - see front matter © 2012 Elsevier Ltd. All rights reserved.
http://dx.doi.org/10.1016/j.ijsolstr.2012.07.022

Author's personal copy

find the onset of the critical buckling load and associated eigenmode in an infinite, periodic solid and determine its nature (i.e. local or global), is the use of the Bloch wave representation theorem (see (Bloch, 1928)). This theoretical tool has allowed the study of the onset of failure for structures involving different types of microgeometries and rate-independent constitutive laws, from layered composites (see (Triantafyllidis and Maker, 1985; Nestorovic and Triantafyllidis, 2004)) to honeycomb and cellular solids (see (Triantafyllidis and Schraad, 1998; Gong et al., 2005; Michailidis et al., 2009)) and subsequently to finitely strained porous and fiber-reinforced elastomers (Triantafyllidis et al., 2006; Michel et al., 2007, 2010).

Unlike typical composites used in engineering applications (e.g. graphite-epoxy) that have global critical modes and for which the corresponding Finite Element Method (F.E.M) analyses need only have an imperfection with wavelength commensurate with overall structural dimensions (e.g. see (Kyriakides et al., 1995; Vogler et al., 2000; Drapier et al., 2001)), the application at hand has a local critical mode with a finite wavelength that needs to be determined. The current problem is, to best of the authors knowledge, the first application of the Bloch wave methodology to a full 3*D* continuum problem, which has the added complication of a non-trivial principal solution, due to the presence of bending. Although some simplified structural models have been proposed for this problem, in the spirit of the structural fiber buckling model of Rosen (1965) (e.g. (Francis et al., 2006; Schultz et al., 2007)), the determination of the structure's critical curvature and associated eigenmode follows the continuum approach in Triantafyllidis et al. (2006), appropriately modified for principal solutions of finite bending and 3*D* microstructures. Of course full field micromechanical calculations are always an option, as in Lopez Jiménez and Pellegrino (2012), but the advantage of the proposed method is the direct theoretical determination of the critical wavelength.

The paper is organized as follows: In Section 2 is presented the general setting of the 3*D* problem. Section 3 introduces the principal solution of the infinite, periodic structure, followed by the 2*D* onset of bifurcation analysis based on the Bloch wave representation of the eigenmode. The F.E.M.-based numerical solution procedure for the 2*D* model, which determines the critical curvature and associated eigenmode is given in Section 4. Numerical results from the full 3*D* calculations of an imperfect, finite model based on a homogenized model for the ply proposed by Le Tallec et al. (2012) plus experimental results are presented and compared in Section 5. The paper ends with a discussion in Section 6.

2. Problem setting

This section presents the mechanical problem under consideration. It is divided into two parts, starting with the presentation of the structure's geometry and experimental set-up and continuing with the description of the general problem setting in 3*D*.

2.1. Structure's geometry and experimental set-up

The experiments pertain to the pure bending of a long rubber slab of initial length L_1 with a rectangular cross section of dimensions $L_2 \times (H-t)$, where $L_1 > L_2 > (H-t)$. A thin metallic plate of dimensions $L_1 \times L_2 \times t$ is glued on the top side of the slab, as depicted in Fig. 1. The slab is reinforced by a layer (also termed "*ply*") of thin metallic cables (also termed "*fibers*") of radius r, separated from each other by a constant gap e, at a distance h from the bottom free edge and running across its entire length. In its undeformed, stress-free configuration the structure occupies a volume Ω in $\mathbb{R}^3$, where material points are identified by their reference Cartesian coordinates X_i. The structure is periodic along the X_2 direction with an L_1-long unit cell of cross-section Y of dimensions $e \times H$, as shown also in Fig. 1.

A state of pure bending is imposed to the structure by applying opposite moments at the two ends of the structure $X_1 = \pm L_1/2$, as shown in Fig. 4, whereas all the other boundaries remain free. For relatively small values of the applied moments, the structure assumes a cylindrical configuration with a generator along the X_2 direction as seen in Fig. 2. This is the principal solution of the structure, which has a stress state independent of X_1 and is Y-periodic in X_2 for an adequately large number of fibers, ignoring of course edge effects along $X_2 = \pm L_2/2$.

Due to the applied pure bending, the metal plate is in tension and the ply is in compression, which in view of the assumed perfect bonding between matrix and fibers, imposes a compressive stress on the surrounding rubber matrix. The large difference in stiffness between matrix and fibers destabilizes the composite by fiber rotation about the X_3 direction, leading to an overall buckling of the structure in the (X_1, X_2) plane, as seen in Fig. 3.

Finding the critical curvature for the onset of the lateral buckling and the corresponding eigenmode's wavelength is the object of the this work, as subsequently detailed.

2.2. General problem setting in 3D

The 3*D* boundary value problem is presented here by giving the energy density of the different constituents of the structure and its essential (kinematic) boundary conditions.

Standard notational conventions apply, with $\boldsymbol{x}(\boldsymbol{X})$ denoting the position vector of a material point in the current (reference) configuration, $\boldsymbol{u}(\boldsymbol{X})$ the corresponding displacement, $\boldsymbol{F}$ the deformation gradient, $\boldsymbol{C}$ the right Cauchy–Green tensor, $\boldsymbol{E}$ the Lagrangian strain measure, namely:

$$\boldsymbol{u} \equiv \boldsymbol{x}(\boldsymbol{X}) - \boldsymbol{X}, \quad \boldsymbol{F} \equiv \boldsymbol{x}\nabla, \quad \boldsymbol{C} \equiv \boldsymbol{F}^T \cdot \boldsymbol{F}, \quad \boldsymbol{E} \equiv \frac{1}{2}(\boldsymbol{C} - \boldsymbol{I}). \tag{1}$$

The structure's energy $\mathcal{E}(\boldsymbol{u})$ is given by:

$$\mathcal{E}(\boldsymbol{u}) = \int_\Omega W(\boldsymbol{X}, \boldsymbol{E})\, d\boldsymbol{X}, \tag{2}$$

where the domain Ω is the $L_1 \times L_2 \times H$ parallelepiped in $\mathbb{R}^3$. It will be assumed that the rubber matrix, as well as the metallic plate and steel cables are isotropic, thus making their corresponding energy density functions W dependent on the invariants of $\boldsymbol{C}$ (or $\boldsymbol{E}$):

$$\begin{aligned} I_1 &= \mathrm{Tr}(\boldsymbol{C}) = 2\,\mathrm{Tr}(\boldsymbol{E}) + 3, \\ I_2 &= \frac{1}{2}\left[\mathrm{Tr}(\boldsymbol{C}^2) - (\mathrm{Tr}(\boldsymbol{C}))^2\right] = 3 + 4\,\mathrm{Tr}(\boldsymbol{E}) + 2\left[\mathrm{Tr}(\boldsymbol{E}^2) - (\mathrm{Tr}(\boldsymbol{E}))^2\right], \\ I_3 &= \det(\boldsymbol{C}) = \det(\boldsymbol{I} + 2\boldsymbol{E}). \end{aligned} \tag{3}$$

Consequently the energy density $W(\boldsymbol{X}, \boldsymbol{E})$ in (2), which is independent on X_1, takes – depending on the location of the material point of the material point (X_2, X_3) on the unit cell – the form:

$$W = W(\boldsymbol{X}, \boldsymbol{E}) = \begin{cases} W_{plate}(\boldsymbol{E}), \\ W_{rubber}(\boldsymbol{E}), \\ W_{cable}(\boldsymbol{E}), \end{cases} \tag{4}$$

which we specify herein as:

$$\begin{aligned} W_{rubber} &= C_1(I_1 - 3 - \ln(I_3)) + C_2(I_2 - 3 - 2\ln(I_3)) + \frac{\kappa}{2}\left(\sqrt{I_3} - 1\right)^2, \\ W_{cable},\ W_{plate} &= \frac{E}{2(1+\nu)}\left[\mathrm{Tr}(\boldsymbol{E}^2) + \frac{\nu}{1-2\nu}(\mathrm{Tr}(\boldsymbol{E}))^2\right], \end{aligned} \tag{5}$$

where C_1, C_2, κ are the constants for the rubber's compressible Mooney-type model and E, ν are respectively the Young's modulus and Poisson ratio of the corresponding metal.

Author's personal copy

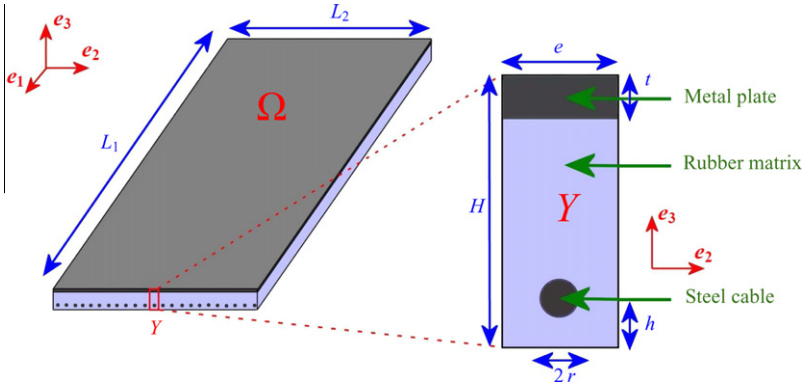

Fig. 1. Reference (stress-free) configuration geometry of the fiber-reinforced rubber slab glued on a thin metal plate and detail of the cross-section Y of its unit cell.

Fig. 2. Principal solution of the fiber-reinforced rubber slab bonded on a thin metal plate and subjected to pure bending. (Photo courtesy of Astier and Caillard (2006)).

Fig. 3. Buckled state of the fiber-reinforced rubber slab bonded on a thin metal plate and subjected to pure bending. (Photo courtesy of Astier and Caillard (2006)).

Equilibrium is obtained by extremizing $\mathcal{E}(\boldsymbol{u})$ with respect to the displacement field $\boldsymbol{u}$, namely:

$$\mathcal{E}_{,\boldsymbol{u}}(\boldsymbol{\delta u}) = \int_{\Omega} (W_{\boldsymbol{F}} : \boldsymbol{\delta F})\, d\boldsymbol{X} = 0. \tag{6}$$

To the above equilibrium equations in weak form, we must add the essential (kinematic) boundary conditions for $\boldsymbol{u}$. Pure bending can be achieved by rotating the two end-sections of the slab ($X_1 = \pm L_1/2$) by an angle $\theta_0 = \rho L_1$, where ρ is the curvature imposed on the slab (i.e. undeformed fiber's inverse radius). The two end faces are kept flat and shear free. The corresponding kinematic constraint imposed at the two ends is:

$$\boldsymbol{u}(X_1, X_2, X_3) \cdot [\cos(\rho X_1)\boldsymbol{e}_1 - \sin(\rho X_1)\boldsymbol{e}_3] = 0, \quad X_1 = \pm L_1/2. \tag{7}$$

The above kinematic condition is also compatible with an X_1-independent principal solution in the case of a perfect structure with $W(X_2, X_3, \boldsymbol{E})$ as discussed in the next section. A schematic diagram of an (X_1, X_3) section of the deformed configuration (principal solution) for a perfect structure is shown in Fig. 4.

One final, but obvious detail: to avoid X_2 translation indeterminacy of the solution of (6), (7), the rigid body motion along $\boldsymbol{e}_2$ is eliminated by constraining the X_2-displacement at some point of the $X_1 = -L_1/2$ face.

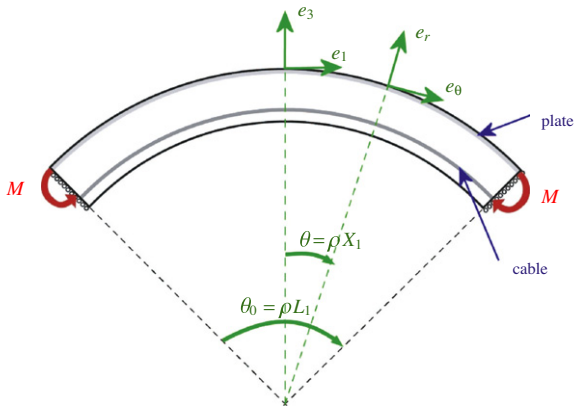

Fig. 4. Schematic representation of the principal solution and the kinematic boundary conditions applied to the structure.

3. Stability of the infinite perfect structure

This section pertains to the stability of an infinite, perfect structure subjected to pure bending. By assuming a structure with X_1-independent energy densities, i.e. $W(X_2, X_3, \boldsymbol{E})$, and where in addition we have $e \ll L_2$, i.e. many unit cells along the X_2 direction, one obtains by ignoring edge effects of the finite structure an

Author's personal copy

X_2-periodic (and X_1-independent) principal solution of (6), (7). The stability of this principal solution is examined with the help of Bloch wave representation theory for the 3*D* eigenmode, which requires the solution of a 2*D* problem defined on the cross-section of the unit cell Y (see Fig. 1). A full Lagrangian formulation of the 3*D* stability problem is used here, which leads naturally to the consideration of a 2*D* problem on the reference configuration unit cell Y set in Cartesian coordinates. The advantage of this approach lies in the use of Cartesian coordinates, in spite of a cylindrically deformed principal solution.

3.1. Principal solution

The structure's principal solution corresponds to the bending of a rectangular parallelipiped into a cylindrical tube segment with axis along $\boldsymbol{e}_2$ (see the corresponding deformed (X_1,X_3) plane section in Fig. 4) and and where the sections $X_1 = \text{const.}$ deform only into their own plane, i.e. remain flat. Consequently the displacements $\boldsymbol{u}$ can be written as:

$$\boldsymbol{u}(X_1,X_2,X_3) = \boldsymbol{R}(\rho X_1)\,.\,\boldsymbol{u}(0,X_2,X_3), \tag{8}$$

where $\boldsymbol{R}$ is the rigid body rotation tensor of the plane $X_1 = \text{const.}$, i.e.

$$\begin{aligned}&\boldsymbol{R} \equiv \boldsymbol{e}_\theta \otimes \boldsymbol{e}_1 + \boldsymbol{e}_2 \otimes \boldsymbol{e}_2 + \boldsymbol{e}_r \otimes \boldsymbol{e}_3;\\ &\boldsymbol{e}_\theta \equiv \boldsymbol{e}_1 \cos(\rho X_1) - \boldsymbol{e}_3 \sin(\rho X_1),\\ &\boldsymbol{e}_r \equiv \boldsymbol{e}_1 \sin(\rho X_1) + \boldsymbol{e}_3 \cos(\rho X_1).\end{aligned} \tag{9}$$

Note that the principal solution displacement $\boldsymbol{u}(0,X_2,X_3)$ is taken to be X_2-periodic:

$$\boldsymbol{u}(0,X_2,X_3) \equiv \boldsymbol{p}(X_2,X_3) = \boldsymbol{p}(X_2 + ne,X_3); \quad n \in \mathbb{Z}. \tag{10}$$

Consequently, using (9) and (8) into the definition of the deformation gradient, one obtains:

$$\begin{aligned}&\boldsymbol{\delta u}\boldsymbol{\nabla} = \boldsymbol{R}(\rho X_1)\,.\,\left[\boldsymbol{A}\,.\,\boldsymbol{\delta p} \otimes \boldsymbol{e}_1 + \boldsymbol{\delta p}_{,2} \otimes \boldsymbol{e}_2 + \boldsymbol{\delta p}_{,3} \otimes \boldsymbol{e}_3\right];\\ &\boldsymbol{A} \equiv \rho[\boldsymbol{e}_1 \otimes \boldsymbol{e}_3 - \boldsymbol{e}_3 \otimes \boldsymbol{e}_1].\end{aligned} \tag{11}$$

Substituting (11) into the equilibrium Eq. (6) and taking (8) into account, one finally obtains the following characterization of the principal solution $\boldsymbol{p}(X_2,X_3)$:

$$\int_Y W_{,\boldsymbol{F}} : \left[\boldsymbol{A}\,.\,\boldsymbol{\delta p} \otimes \boldsymbol{e}_1 + \boldsymbol{\delta p}_{,2} \otimes \boldsymbol{e}_2 + \boldsymbol{\delta p}_{,3} \otimes \boldsymbol{e}_3\right] dX_2 dX_3 = 0, \tag{12}$$

over all X_2-periodic functions $\boldsymbol{p}$ defined on Y, to which one must add the kinematic condition:

$$\boldsymbol{p}\,.\,\boldsymbol{e}_1 = p_1(X_2,X_3) = 0, \tag{13}$$

which simply states that the $X_1 = 0$ section remains flat.

Finally an interesting remark is in order. By choosing $\delta\boldsymbol{p} = c\,\boldsymbol{e}_3$, where $c \neq 0$ is an arbitrary constant, (12) yields:

$$N \equiv \int_Y W_{,F_{11}}\, dX_2 dX_3 = 0, \tag{14}$$

where N is the axial force on the section Y (since $W_{,F_{11}} \equiv \Pi_{11}$ is the corresponding normal component of the first Piola–Kirchhoff stress).

3.2. Stability of the principal solution

All equilibrium solutions of the (conservative, elastic) structure with energy $\mathcal{E}(\rho,\boldsymbol{u})$ in (2) are given by the first functional derivative of this energy with respect to $\boldsymbol{u}$, according to (6). For each value of the applied curvature ρ, there is a principal solution:

$$\overset{0}{\boldsymbol{u}}(\rho;X_1,X_2,X_3) = \boldsymbol{R}(\rho X_1)\,.\,\boldsymbol{p}(\rho;X_2,X_3), \tag{15}$$

where $\boldsymbol{p}$ is the X_2-periodic (and X_1-independent) equilibrium solution on the unit cell given by (12) and (13).

The stability of the above solution depends on whether the principal solution $\overset{0}{\boldsymbol{u}}(\rho;\boldsymbol{X})$ is a local minimum of the structure's energy. A sufficient condition for this minimum is a positive lowest eigenvalue $\beta(\rho)$ for the stability operator $\mathcal{E}_{,\boldsymbol{uu}}(\Delta\boldsymbol{u},\Delta\boldsymbol{u})$ evaluated on $\overset{0}{\boldsymbol{u}}(\rho;\boldsymbol{X})$:

$$\begin{aligned}&\beta(\rho) = \inf_{\|\Delta\boldsymbol{u}\boldsymbol{\nabla}\|=1} \mathcal{E}_{,\boldsymbol{uu}}(\Delta\boldsymbol{u},\Delta\boldsymbol{u}) = \inf_{\|\Delta\boldsymbol{u}\boldsymbol{\nabla}\|=1} \mathcal{F}_\Omega(\Delta\boldsymbol{u}\boldsymbol{\nabla});\\ &\mathcal{F}_\Omega(\boldsymbol{g}) \equiv \int_\Omega \bar{\boldsymbol{g}} : W_{,\boldsymbol{FF}} : \boldsymbol{g}\, d\boldsymbol{X},\end{aligned} \tag{16}$$

where $\mathcal{F}_\Omega(\boldsymbol{g})$ denotes a bilinear operator on a rank two tensor $\boldsymbol{g}(\boldsymbol{X})$ defined on Ω and where the rank four tangent moduli tensor $W_{,\boldsymbol{FF}}$ (second derivative of W with respect to $\boldsymbol{F}$) is evaluated on the principal solution.[1]

The X_1-independence and X_2-periodicity of the principal solution $\overset{0}{\boldsymbol{u}}$ imply the same properties for $W_{,\boldsymbol{FF}}$ which is evaluated on $\overset{0}{\boldsymbol{u}}$. Consequently it can be shown (by a small modification of the results in Geymonat et al. (1993)) that the eigenmode of (16) has the following Bloch wave representation:

$$\Delta\boldsymbol{u}(X_1,X_2,X_3) = \exp(i\omega_1 X_1 + i\omega_2 X_2)\,\boldsymbol{R}(\rho X_1)\,.\,\Delta\boldsymbol{p}(X_2,X_3), \tag{17}$$

where $\Delta\boldsymbol{p}$ is an X_2-periodic function defined in Y and $(\omega_1,\omega_2) \in \mathbb{R}^+ \times [0,2\pi/e)$. A numerically more convenient choice uses the representation:

$$\begin{aligned}&\Delta\boldsymbol{u}(X_1,X_2,X_3) = \exp(i\omega_1 X_1)\,\boldsymbol{R}(\rho X_1)\,.\,\Delta\boldsymbol{q}(X_2,X_3);\\ &\Delta\boldsymbol{q}(X_2,X_3) = \exp(i\omega_2 X_2)\,\Delta\boldsymbol{p}(X_2,X_3)\end{aligned} \tag{18}$$

from which one finds out the following expression for $\Delta\boldsymbol{u}\boldsymbol{\nabla}$:

$$\begin{aligned}\Delta\boldsymbol{u}\boldsymbol{\nabla} = \exp(i\omega_1 X_1)&\boldsymbol{R}(\rho X_1)\\ &\,.\,\left[(\boldsymbol{A}\,.\,\Delta\boldsymbol{q} + i\omega_1\Delta\boldsymbol{q}) \otimes \boldsymbol{e}_1 + \Delta\boldsymbol{q}_{,2} \otimes \boldsymbol{e}_2 + \Delta\boldsymbol{q}_{,3} \otimes \boldsymbol{e}_3\right],\end{aligned} \tag{19}$$

where $\boldsymbol{A}$ is defined in (11).

The calculation of the minimum eigenvalue $\beta(\rho)$ using $\Delta\boldsymbol{u}\boldsymbol{\nabla}$ in (19) involves complex numbers. To avoid them we use the decomposition of $\Delta\boldsymbol{q}$ into real and imaginary part:

$$\Delta\boldsymbol{q} = \Delta\boldsymbol{v} + i\Delta\boldsymbol{w}. \tag{20}$$

Consequently the calculation of $\beta(\rho)$ requires the use of only real fields $\Delta\boldsymbol{v},\Delta\boldsymbol{w}$ defined on Y, namely:

$$\beta(\rho) = \inf_{\|\Delta\boldsymbol{u}\boldsymbol{\nabla}\|=1} [\mathcal{F}_Y(\boldsymbol{G}_{\boldsymbol{v}}) + \mathcal{F}_Y(\boldsymbol{G}_{\boldsymbol{w}})], \tag{21}$$

$$\boldsymbol{G}_{\boldsymbol{v}} = (\boldsymbol{A}\,.\,\Delta\boldsymbol{v} - \omega_1\Delta\boldsymbol{w}) \otimes \boldsymbol{e}_1 + \Delta\boldsymbol{v}_{,2} \otimes \boldsymbol{e}_2 + \Delta\boldsymbol{v}_{,3} \otimes \boldsymbol{e}_3, \tag{22}$$

$$\boldsymbol{G}_{\boldsymbol{w}} = (\boldsymbol{A}\,.\,\Delta\boldsymbol{w} + \omega_1\Delta\boldsymbol{v}) \otimes \boldsymbol{e}_1 + \Delta\boldsymbol{w}_{,2} \otimes \boldsymbol{e}_2 + \Delta\boldsymbol{w}_{,3} \otimes \boldsymbol{e}_3, \tag{23}$$

subject to the following kinematic coupling constraint between $\Delta\boldsymbol{v}$ and $\Delta\boldsymbol{w}$ which follows from (18) and (20):

$$\begin{aligned}&\Delta\boldsymbol{v}(e/2,X_3) = \cos(\omega_2 e)\Delta\boldsymbol{v}(-e/2,X_3) + \sin(\omega_2 e)\Delta\boldsymbol{w}(-e/2,X_3),\\ &\Delta\boldsymbol{w}(e/2,X_3) = \cos(\omega_2 e)\Delta\boldsymbol{w}(-e/2,X_3) - \sin(\omega_2 e)\Delta\boldsymbol{v}(-e/2,X_3).\end{aligned} \tag{24}$$

Of interest here is the lowest value of curvature ρ for which the stability operator $\mathcal{E}_{,\boldsymbol{uu}}(\Delta\boldsymbol{u},\Delta\boldsymbol{u})$ loses its positive definiteness and the associated eigenmode in (17), characterized by the values (ω_1^c,ω_2^c). To this end, we characterize the infimum in (16) as an infimum with respect to all possible wavenumbers (ω_1,ω_2):

$$\beta(\rho) = \inf_{(\omega_1,\omega_2)\in\mathbb{R}^+\times[0,2\pi/e)} \{\gamma(\rho,\omega_1,\omega_2)\} \tag{25}$$

[1] NOTE: $\bar{\boldsymbol{g}}$ denotes the complex conjugate of $\boldsymbol{g}$.

Author's personal copy

of the minimal eigenvalue $\gamma(\rho,\omega_1,\omega_2)$ defined for a given wavenumber pair (ω_1,ω_2) by:

$$\gamma(\rho,\omega_1,\omega_2)=\min_{\substack{\Delta\boldsymbol{v}(\omega_2),\Delta\boldsymbol{w}(\omega_2)\\ \|\Delta\boldsymbol{u}\nabla\|=1}}\{\mathcal{F}_Y(\rho,\boldsymbol{G}_{\boldsymbol{v}}(\rho,\omega_1,\Delta\boldsymbol{v}(\omega_2),\Delta\boldsymbol{w}(\omega_2)))+\mathcal{F}_Y(\rho,\boldsymbol{G}_{\boldsymbol{w}}(\rho,\omega_1,\Delta\boldsymbol{v}(\omega_2),\Delta\boldsymbol{w}(\omega_2)))\}. \tag{26}$$

Defining $\rho_m(\omega_1,\omega_2)$ as the lowest curvature where we reach a zero eigenvalue β of the stability operator for a given wavenumber pair (ω_1,ω_2):

$$\rho_m(\omega_1,\omega_2)=\inf_{\gamma(\rho,\omega_1,\omega_2)=0}\rho, \tag{27}$$

the sought critical curvature is:

$$\rho_c\equiv\inf_{(\omega_1,\omega_2)\in\mathbb{R}^+\times[0,2\pi/e)}\rho_m(\omega_1,\omega_2). \tag{28}$$

The above definition for the critical curvature ρ_c leads naturally to the numerical algorithm for its calculation, as detailed in the next section.

4. Solution procedure

The numerical algorithm used is presented in this section, starting with the part on the unit cell discretization and corresponding principal solution, and following with part pertaining to the critical curvature and associated eigenmode. The calculations use the finite element software `Freefem++` (see http://www.freefem.org/ff++/).

4.1. Unit cell discretization and principal solution

The starting point for calculating the principal solution displacement field $\boldsymbol{p}(X_2,X_3)$ in (10) is the weak form of the equilibrium Eq. (12) subject to (13). The N-node F.E.M. discretization of the 2D unit cell Y is based on 6-node triangular elements (with nodes at vertices and mid-points of sides) as shown in Fig. 5. In the interest of computational simplicity the field $\boldsymbol{\delta b}\equiv\boldsymbol{A}\,.\,\boldsymbol{\delta p}$ is discretized independently of the field $\boldsymbol{\delta p}$ (see expression for $\boldsymbol{\delta F}$ in (11)), thus resulting in elements with 6 d.o.f. per node (three for the $\boldsymbol{p}$ components and three for the $\boldsymbol{b}$ components). Linear relationships between $\boldsymbol{\delta b}$ and $\boldsymbol{\delta p}$ are introduced subsequently, thus reducing the total number of $\boldsymbol{p}$-related variables to 3N and then to 2N, since according to (13) $p_1=0$. Periodicity of $\boldsymbol{p}$ (see (10)) couples the nodes on the left (Γ_L) and right (Γ_R) boundary sides of Y, thus explaining the common X_3 coordinate between the corresponding nodes in each side. The F.E.M discretization uses 263 elements with a total of $N=568$ nodes.

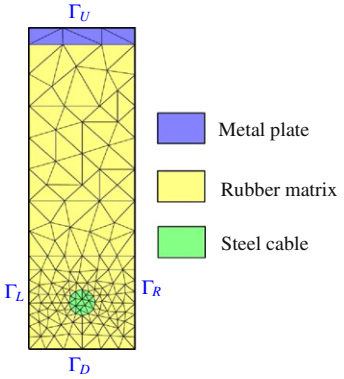

Fig. 5. Unit cell Y discretization is based on a triangular element mesh with quadratic polynomial interpolation resulting in 6-node triangular elements.

Table 1
Material constants used in numerical calculations.

Metal plate		Rubber matrix		Steel cables	
E_{plate}	210 GPa	C_1	0.9774 MPa	E_{cable}	154.3 GPa
ν_{plate}	0.3	C_2	0.1086 MPa	ν_{cable}	0.3
		κ	1000 MPa		

An incremental Newton–Raphson algorithm, using the curvature ρ as its loading parameter, is used to find the principal solution. The corresponding discretized "*stiffness*" matrix $[\boldsymbol{K}(\rho)]$, based upon the interpolation of the two independent fields $\boldsymbol{b}$ and $\boldsymbol{p}$ as previously explained, is used in the stability calculations as described next. The step size used in finding the principal solution is $\Delta\rho=5\times10^{-6}$ rad mm^{-1} and a tolerance of 1×10^{-10} based on the norm of $\Delta\boldsymbol{p}$ is used for the convergence resulting in about 5 iterations per step.

4.2. Critical curvature and eigenmode calculation

The starting point for calculating the critical curvature and corresponding eigenmode is the discretization of the fields $\Delta\boldsymbol{v}$ and $\Delta\boldsymbol{w}$ in the quadratic functional given in (21), which is the sum of two terms of the type $[\boldsymbol{G}]^T[\boldsymbol{K}(\rho)][\boldsymbol{G}]$. In the latter expression the linear operator $[\boldsymbol{G}](\Delta\boldsymbol{b},\Delta\boldsymbol{p})$ is first the F.E.M. discretization of $\boldsymbol{G}_{\boldsymbol{v}}$ in (21) with $\Delta\boldsymbol{b}\equiv\boldsymbol{A}\,.\,\Delta\boldsymbol{v}-\omega_1\Delta\boldsymbol{w}$, $\Delta\boldsymbol{p}\equiv\Delta\boldsymbol{v}$ and next the F.E.M. discretization of $\boldsymbol{G}_{\boldsymbol{w}}$ in (21) with $\Delta\boldsymbol{b}\equiv\boldsymbol{A}\,.\,\Delta\boldsymbol{w}+\omega_1\Delta\boldsymbol{v}$, $\Delta\boldsymbol{p}\equiv\Delta\boldsymbol{w}$. As a result, the quadratic form in (21) can be written as:

$$\mathcal{F}_Y=[\Delta\boldsymbol{q}]^T[\hat{\boldsymbol{G}}(\omega_1)]^T[\hat{\boldsymbol{K}}(\rho)][\hat{\boldsymbol{G}}(\omega_1)][\Delta\boldsymbol{q}];\quad[\Delta\boldsymbol{q}]\equiv([\Delta\boldsymbol{v}],[\Delta\boldsymbol{w}]), \tag{29}$$

where the discretized stiffness matrix $\hat{\boldsymbol{K}}(\rho)$ has 6N d.o.f. (recall that N is the total number of nodes). The last step in the construction of the matrix corresponding to the quadratic form in (21) is the ω_2-dependent relation between the Γ_L,Γ_R sides of the unit cell boundary values of $[\Delta\boldsymbol{v}]$ and $[\Delta\boldsymbol{w}]$. This relation is expressed by the linear system $[\Delta\boldsymbol{q}]=[\hat{\boldsymbol{H}}(\omega_2)][\Delta\hat{\boldsymbol{q}}]$, where $\Delta\hat{\boldsymbol{q}}$ are the independent degrees of freedom of the system, i.e. the nodal values of $\Delta\boldsymbol{v}$, $\Delta\boldsymbol{w}$ (real and imaginary part of $\Delta\boldsymbol{q}$ defined in (18) and (20)) on all nodes of the unit cell Y except those on the Γ_R side of its boundary. Consequently, the discrete version of the functional in (26) becomes[2]:

$$\gamma(\rho,\omega_1,\omega_2)=\min_{\|\Delta\hat{\boldsymbol{q}}\|=1}[\Delta\hat{\boldsymbol{q}}]^T[\mathbb{K}(\rho,\omega_1,\omega_2)][\Delta\hat{\boldsymbol{q}}];$$
$$[\mathbb{K}(\rho,\omega_1,\omega_2)]\equiv[\hat{\boldsymbol{H}}(\omega_2)]^T[\hat{\boldsymbol{G}}(\omega_1)]^T[\hat{\boldsymbol{K}}(\rho)][\hat{\boldsymbol{G}}(\omega_1)][\hat{\boldsymbol{H}}(\omega_2)]. \tag{30}$$

For a given curvature ρ and pair $(\omega_1,\omega_2)\in\mathbb{R}^+\times[0,2\pi/e)$, the minimum eigenvalue γ of $[\mathbb{K}]$ is calculated by the shifted inverse power method (e.g. see (Mathews and Fink, 2004)). For $0\leqslant\rho<\rho_c$, $\gamma(\rho,\omega_1,\omega_2)>0\ \forall(\omega_1,\omega_2)\in\mathbb{R}^+\times[0,2\pi/e)$.

The algorithm used here consists of finding lowest positive root $\rho_m(\omega_1,\omega_2)$ of $\gamma=0$ for each pair (ω_1,ω_2) according to (27), resulting in a numerical evaluation of the surface $\rho_m(\omega_1,\omega_2)$ which is then used to find ρ_c according to (28). The scanning of the (ω_1,ω_2) domain used $\omega_1^{max}=0.23$ rad mm^{-1} and step sizes $\Delta\omega_1=0.005$ rad mm^{-1}, $\Delta\omega_2=0.314$ rad mm^{-1} while the curvature was increased by increments $\Delta\rho=5\times10^{-6}$ rad mm^{-1}. The algorithm is given below:

[2] NOTE: Since we are only interested in the roots of γ, the selection of the norm for the discretized mode $\Delta\boldsymbol{u}$ is irrelevant, thus motivating the simpler norm choice of $\|\Delta\hat{\boldsymbol{q}}\|$ instead of the one resulting from the definition in (16).

Author's personal copy

Algorithm 1. Algorithm to compute the critical curvature and corresponding eigenmode

```
Initialize each element of the array ρ_m(:,:) to ρ_max + 1
for ρ from 0 to ρ_max do
      Compute the equilibrium using an incremental Newton–Raphson method ⇒ K(ρ)
  for ω1 from 0 to ω1^max do
    for ω2 from 0 to 2π/e do
      if ρ_m(ω1, ω2) > ρ then
        Compute [Ĝ(ω1)] and [Ĥ(ω2)]
        Build 𝕂(ρ, ω1, ω2) using expression (30)
        Compute γ(ρ, ω1, ω2) defined by (30) using an inverse power method
        if γ(ρ, ω1, ω2) ⩽ 0 then
          ρ_m(ω1, ω2) = ρ
        else
          Instability already found
        end
      end
    end
  end
end
Output: Array ρ_m(:,:)
```

Calculation of the critical eigenmode is a straightforward matter consisting on obtaining $\Delta\boldsymbol{v}$ (or $\Delta\boldsymbol{w}$), over the entire unit cell, corresponding to (ω_1^c, ω_2^c).

Finally a comment is here in order about the algorithm used, which essentially consists of finding the level sets $\gamma = 0$ for each curvature ρ over the (ω_1, ω_2) domain $(0, \omega_1^{max}] \times [0, 2\pi/e)$. This approach is dictated by computational efficiency since it is much less time consuming to calculate $[\mathbb{K}(\rho, \omega_1, \omega_2)]$ based on $[\boldsymbol{K}(\rho)]$ for each fixed ρ on a (ω_1, ω_2) grid than recalculating $[\boldsymbol{K}(\rho)]$ at each value of ρ in the range $[0; \rho_m]$ for each fixed pair (ω_1, ω_2).

5. Results and discussion

The numerical results leading to the calculation of the critical curvature and the corresponding eigenmode, obtained via the procedure outlined in Sections 3 and 4, are hereby compared with experimental data as well as F.E.M. results of the 3*D* model.

5.1. Geometry and material properties

The tests are performed on a reinforced rubber/steel plate assembly which at rest is a rectangular parallelepiped with length $L_1 = 300$ mm, width $L_2 = 20$ mm and height $H = 7.61$ mm. The steel plate has thickness $t = 0.4$ mm and the elastomer's reinforcing steel cables have a radius $r = 0.3115$ mm and are placed at a distance $h = 1.105$ mm from the closest free surface and separated from each other by $e = 2.5$ mm. The material constants of the constitutive laws (5) for the different components of the specimen are given below in Table 1.

5.2. Results for the infinite, perfect structure (based on a 2D model of the unit cell Y)

The solution procedure requires the calculation of the principal solution (on the unit cell *Y*) over a range of curvatures ρ, starting at $\rho = 0$ and proceeding by small increments $\Delta\rho$. It is instructive to show a corresponding typical stress state, which for the case of a dimensionless curvature $\rho H = 7.61 \times 10^{-4}$ is depicted in Fig. 6.

More specifically Fig. 6(a) records the out-of-plane axial component σ_{11} of the Cauchy stress while Fig. 6(b) records the in-plane shear component σ_{23} of the Cauchy stress. As expected from the state of pure bending of the principal solution, the largest compressive axial stress occurs at the cable and the largest tensile axial stress occurs at the plate, while considerably lower axial stresses exist in the rubber matrix. Notice that the in-plane shear stresses σ_{23} are negligible compared to σ_{11}, as expected from the several order of magnitude difference between the shear moduli of the rubber matrix and steel plate and cables. In addition, principal solution equilibrium considerations of the unit cell, i.e. a zero total transverse shear resultant in the (X_2, X_3) plane, explain the antisymmetry of σ_{23} with respect to X_3-axis and the negligible shear force exerted on the cable along that direction.

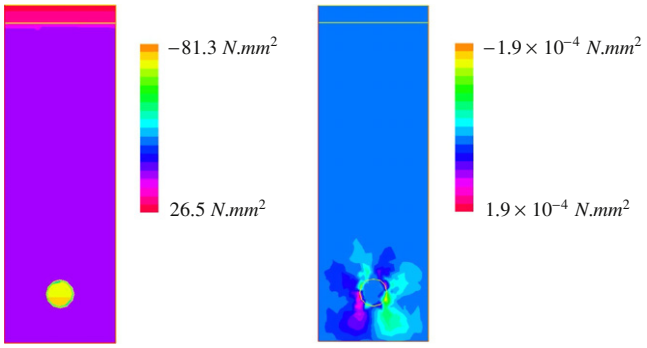

(a) Contours of σ_{11} (b) Contours of σ_{23}

Fig. 6. Principal solution contours of the Cauchy stress axial component σ_{11} in (a) and shear component σ_{23} in (b) plotted on the unit cell *Y* for a dimensionless curvature $\rho H = 7.61 \times 10^{-4}$.

The numerically calculated surface $\rho_m(\omega_1, \omega_2)$, which is the minimum onset of bifurcation curvature as a function of the wavenumbers along the X_1 and X_2 directions, is shown in Fig. 7.

Notice that the surface $\rho_m(\omega_1, \omega_2)$ is symmetric about the $\omega_2 = \pi/e$ plane, as expected from the X_3-symmetry of the unit cell. The minimum over (ω_1, ω_2) critical curvature ρ_c occurs for the X_2-periodic modes, i.e. for $\omega_2 e = 0 \ (mod\ 2\pi)$. Upon a closer inspection (see insert in Fig. 7), the critical curvature ρ_c and the associated wavenumbers ω_1^c, ω_2^c are found to be:

$$\omega_1^c = 0.175 \text{ rad mm}^{-1},\ \omega_2^c = 0 \text{ rad mm}^{-1};$$
$$\rho_c = 3.36 \times 10^{-4} \text{ mm}^{-1}. \tag{31}$$

Based on the above results, the critical wavelength in the X_1-direction is $L_1^c = 2\pi/\omega_1^c = 34.9$ mm. The corresponding instability mode is plotted in Fig. 8 with the X_2 and X_3 components superimposed on the reference coordinate of each node. The X_1 and X_3 components of the eigenmode are negligible compared to their X_2 counterpart, as illustrated further by the contour plot of the X_3 component. The eigenmode $\Delta\boldsymbol{v}$ plotted here is normalized so that the maximum over *Y* lateral displacement $(\Delta v_2)_{max} = 1.2$ mm. It is worth noticing that the X_2 component is by far the dominant component of the eigenmode, in agreement with experimental observations.

5.3. Results for the finite, imperfect structure (based on the 3D F.E.M. model)

An imperfect, finite size 3D F.E.M. model is also used to calculate the critical curvature and corresponding mode for the specimen used in experiments. A detailed 3D model, with a full discretization of each individual fiber, would be excessively (and unnecessarily for our purpose) time consuming. Consequently, an enriched model of the fiber-reinforced ply, described in Le Tallec et al. (2012), is used consisting of a layer at the plane of the cable axes $X_3^{cable} = h$ of surface energy W_{ply}^s and a surrounding rubber

Author's personal copy

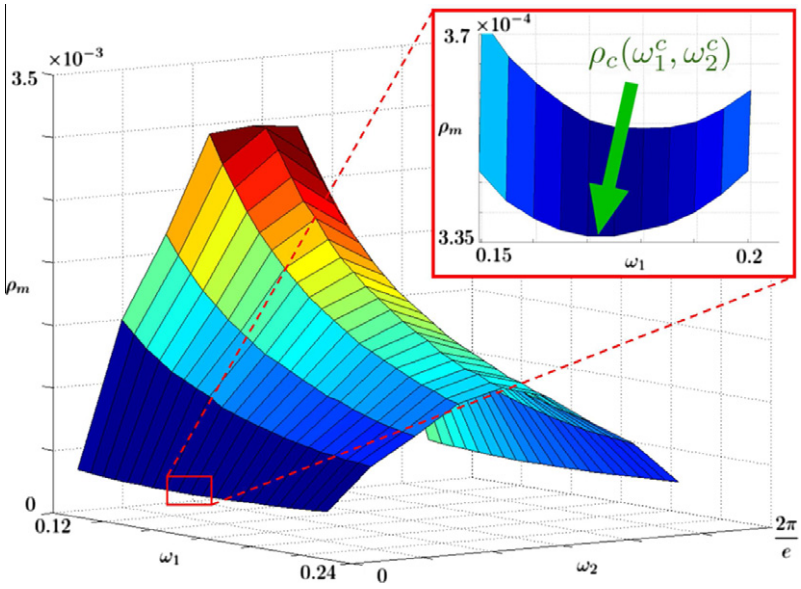

Fig. 7. Numerically calculated surface for the minimum onset of bifurcation curvature $\rho_m(\omega_1,\omega_2)$ as a function of eigenmode wavenumbers ω_1 and ω_2 based on the infinite, perfect periodic 2*D* model.

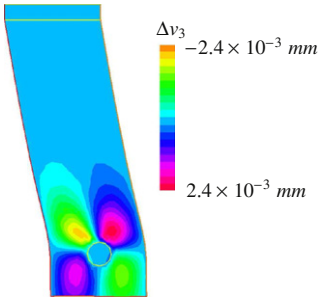

Fig. 8. Critical mode $\Delta\boldsymbol{v}$ depicted by adding its X_2, X_3 components on the reference position of each node. The X_2 is by far the dominant eigenmode component (the much smaller X_3 component is given by a contour plot). Results are based on the infinite, perfect periodic 2*D* model.

matrix layer, also centered at $X_3 = h$, with a thickness l and an energy density W^v_{ply}. The surface energy of the cable layer is given by:

$$W^s_{ply} = \frac{1}{2e}\Big\{EA(\boldsymbol{x}_{,1}\cdot\boldsymbol{d}_1)^2 + GA\Big[(\boldsymbol{x}_{,1}\cdot\boldsymbol{d}_2)^2 + (\boldsymbol{x}_{,1}\cdot\boldsymbol{d}_3)^2\Big] + GJ(\boldsymbol{d}_{2,1}\cdot\boldsymbol{d}_3)^2 + EI\Big[(\boldsymbol{d}_{1,1}\cdot\boldsymbol{d}_3)^2 + (\boldsymbol{d}_{1,1}\cdot\boldsymbol{d}_2)^2\Big]\Big\}, \tag{32}$$

where e denotes the steel cable spacing and $\boldsymbol{d}_i(X_1,X_2,X_3^{cable})$ the corresponding director field. The *EA* term in the above equation accounts for the axial energy, the *GA* terms account for the shear energy, the *GJ* term for the torsional energy and the *EI* terms for the bending energy stored in the cables, where A, J and I are respectively the cross-sectional area, torsional constant and moment of inertia of each cable.

The energy density of the rubber matrix surrounding the cables, in the ply of thickness $l = 0.624\,mm$, is:

$$W^v_{ply} = \frac{1}{1-f_c}W_{rubber};\quad f_c \equiv \frac{A}{el}, \tag{33}$$

where f_c is the volumetric fraction of cable in the ply and W_{rubber} is given in (5). Numerical values of the cable constants in (32) in the ply are given below in Table 2, while the rubber matrix properties are given in Table 1.

The overall dimensions of the 3*D* specimen in the reference configuration are $L_1 = 300$ mm, $L_2 = 20$ mm and $H = 7.61$ mm. The

Table 2
Material constants for the cables in the ply used in numerical calculations.

EA	*GA*	*EI*	*GJ*
47030 N	18090 N	1140 N mm^2	877 N mm^2

model is subjected to pure bending boundary conditions, which in addition to the displacement constraints in (7) requires an analogous set of constraints for the director d.o.f. namely:

$$\boldsymbol{d}_1 = \cos(\rho X_1)\boldsymbol{e}_1 - \sin(\rho X_1)\boldsymbol{e}_3,\quad \boldsymbol{d}_2 = \boldsymbol{e}_2,$$
$$\boldsymbol{d}_3 = \sin(\rho X_1)\boldsymbol{e}_1 + \cos(\rho X_1)\boldsymbol{e}_3;\quad X_1 = \pm L_1/2. \tag{34}$$

The resulting 3*D* F.E.M. model has 5082 nodes for the matrix, 2541 nodes for the plate, and 2541 displacement nodes and 847 rotation nodes for the fiber-reinforced layer. It consists of Q_2 elements for the matrix and Q_2 elements for the cable reinforced layer.

On a final note we must also mention the introduction of an imperfection to the 3*D* model, achieved through a displacement of the perfect structure's reference configuration nodal coordinates by the following amount $\Delta\boldsymbol{X}$:

$$\Delta X_1 = 0,\quad \Delta X_2 = \xi(H - X_3)\cos(\omega_1^c X_1),\quad \Delta X_3 = 0, \tag{35}$$

where ξ denotes the imperfection amplitude and ω_1^c is the critical wavenumber obtained by Bloch wave analysis (see (31)). The imperfection used is not a multiple of the eigenmode, but is chosen as a crude approximation of the critical mode with the same X_1 wavelength.

An incremental Newton–Raphson procedure is used for the numerical solution of the resulting 3*D* F.E.M. model, for four different values of the imperfection amplitude parameter ξ. The results, plotted in the form of maximum lateral deviation along X_2 direction, i.e. $(u_2)_{max} - (u_2)_{min}$, with the max and min taken on the $X_2 = 0$ lateral surface, versus dimensionless curvature ρH are given in Fig. 9.

As expected, the maximum lateral deviation of the $X_2 = 0$ surface follows initially the perfect structure by staying close to zero and increases at the neighborhood of the perfect structure's critical curvature; the lower the imperfection amplitude ξ, the more

Author's personal copy

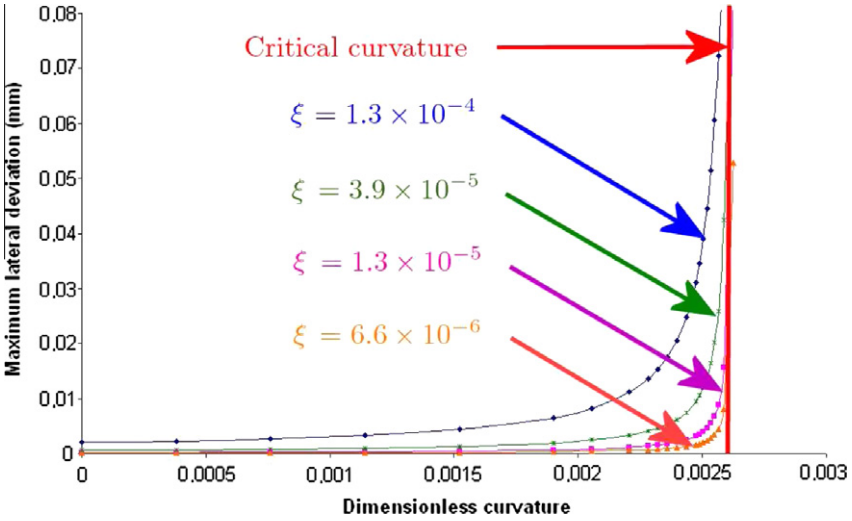

Fig. 9. Maximum lateral deviation of $X_2 = 0$ surface as a function of the dimensionless curvature for different values of the imperfection amplitude, based on the finite, imperfect 3*D* model.

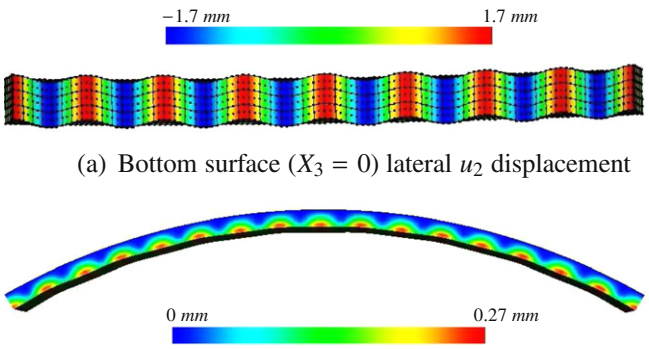

(a) Bottom surface ($X_3 = 0$) lateral u_2 displacement

(b) Lateral surface ($X_2 = 0$) relative radial Δu_r displacement

Fig. 10. Deformation of the 3D imperfect ($\xi = 1.3 \times 10^{-5}$) model at a curvature $\rho H = 2.56 \times 10^{-3}$, showing in (a) the displacement field u_2 on the reference configuration's bottom surface ($X_3 = 0$) and in (b) contours of the radial displacement u_r on the deformed configuration's lateral surface ($X_2 = 0$).

Table 3
Experimental results.

	Critical moment (N mm)	Critical curvature (mm^{-1})	Wavenumber ω_1^c (rad mm^{-1})
Exp. A	3.50×10^3	3.175×10^{-4}	0.167
Exp. B	4.00×10^3	3.322×10^{-4}	0.167
Exp. C	4.24×10^3	3.484×10^{-4}	0.167

Table 4
Comparison of results from two different theoretical models and experiments.

	Critical curvature ($\rho_c H$)	Critical moment (N mm)	Critical mode ω_1^c (rad mm^{-1})
2D Bloch wave analysis	2.557×10^{-3}	4.09×10^3	0.175
3D F.E.M. simulation	2.557×10^{-3}	4.18×10^3	0.178
Experiment	2.528×10^{-3}	3.91×10^3	0.167

abrupt the change, as seen in Fig. 9. The 3*D* numerical calculations serve as an independent and reliable proof of the 2D Bloch wave calculations based on one unit cell.

A plotting of the imperfect (with $\xi = 1.3 \times 10^{-5}$) 3D structure's deformation near the critical curvature, at $\rho H = 2.56 \times 10^{-3}$, is given in Fig. 10. In Fig. 10(a) is plotted the lateral displacement $u_2(X_1, X_2, 0)$ of the bottom surface $X_3 = 0$, while in Fig. 10(b) we plot contours of the relative radial displacement $u_r(X_1, 0, X_3)$ on the lateral surface $X_2 = 0$ (defined by: $\Delta u_r \equiv (\boldsymbol{u}(X_1, 0, H) - \boldsymbol{u}(X_1, 0, X_3)) \cdot (\cos(\rho X_1)\boldsymbol{e}_3 + \sin(\rho X_1)\boldsymbol{e}_1)$).

As expected from the 2D Bloch wave analysis, the 3D structure shows a deformation pattern dominated by an X_1 wavelength very close to the one theoretically predicted by the 2D model. Moreover the buckled pattern in Fig. 10 is essentially a mode in the plane of the reinforcing ply, with a dominant u_2 component, exactly as predicted by the 2D analysis (see also Fig. 8).

5.4. Experimental results and comparison with theoretical predictions

Three different samples, of identical geometric and material properties were tested. Critical curvatures, moments and wavenumbers in X_1 direction are given in Table 3 below.

Notice that the critical wavenumber is insensitive to experimental variation between the three different cases while critical curvatures show a max deviation of 8%. Taking the average value of the three experiments and comparing to the 2*D* Bloch wave calculations for the infinite, perfect model and to the 3*D* calculations for the finite, imperfect model, we end up with the following comparison shown in Table 4.

As expected the analytical results are very close, given the consistency of the modeling approach and the small difference in critical moments and wavenumbers due to the presence of imperfections in the 3D model. What is rather remarkable is the agreement with the experimental results, given the variability of geometry and material properties in the experiments as well as the strong non-uniformity of the strain fields involved.

6. Conclusion

The work presented here pertains to the stability of a fiber-reinforced elastomer (where a row of equally spaced, parallel cables is concentrated in one ply), subjected to constrained (due to an inextensible metallic plate bonded on one side) pure bending. The problem is solved in two different ways: one which assumes that

Author's personal copy

the plate is perfect, infinite and admits a principal solution that is periodic over a 2*D* unit cell *Y*, and the other using an imperfect, finite plate in 3*D*. Of interest is the plate's critical curvature, i.e. the lowest curvature where a bifurcated equilibrium path can be found, and the associated eigenmode.

The results for the perfect, infinite plate require calculations on the F.E.M. discretized 2*D* unit cell *Y*, which make use of the Bloch wave representation theorem for the eigenmode. For the finite plate, the critical curvature and eigenmode are calculated approximately using different amplitude imperfections of critical wavelength and a full 3*D* F.E.M. discretization of the entire plate, with the added simplification of a homogenized model for the ply (developed in Le Tallec et al. (2012)). The critical curvature predictions based on the 2*D* model are found in excellent agreement with those based on its 3*D* counterpart, providing an independent verification of the calculations. Although few experiments were conducted, the critical curvature and eigenmode are in good agreement with the calculations-based predictions.

The main purpose of this work is to demonstrate the power of a theoretical method to accurately determine the critical load and corresponding eigenmode in a class of technologically interesting problems (i.e. problems involving bending in finitely strained fiber-reinforced composites), information that previous work on this subject can only establish approximately either by numerical experiments or by using simple structural models. More specifically, we show how the Bloch wave representation theorem can be used in solving the onset of bifurcation problem at hand by analyzing just the minimum representative domain of the bent structure's principal solution.

There are several novel features here, compared to previous applications of this technique (e.g. (Triantafyllidis et al., 2006; Michel et al., 2007, 2010)): (a) the application of the Bloch wave representation theory to solve a full 3*D* problem (b) the use of a full Lagrangian reference-configuration formulation with Cartesian coordinates that avoids the use of cylindrical coordinates that one might have been tempted to use based on the cylindrical configuration of the principal solution and (c) the associated numerical algorithm that introduces auxiliary variables in order to speed the critical curvature calculations. The methodology presented here can be used for the solution of any bending problem for a fiber-reinforced elastomer. It has the advantage of a direct determination of the critical eigenmode of the structure, which is more reliable than simple structural models (e.g. (Francis et al., 2006)) and thus constitutes a useful ingredient for the 3*D* calculations of the critical curvature since it can avoid numerical experimentation involving large scale 3*D* models (e.g. (Lopez Jiménez and Pellegrino, 2012)).

The problem also opens interesting new questions on the stability of the bifurcated solution found; the 2*D* Bloch wave analysis presented here pertains to the onset of bifurcation while the complementing 3*D* numerical calculations indicate a stable post-bifurcated solution. Numerical simulations on the similar problem by Lopez Jiménez and Pellegrino (2012) also show a stable post-bifurcated solution (moment continuously increasing with curvature) while their experiments show otherwise due to damage, thus making the post-buckling behavior of these composites a worthy topic for further investigation.

Acknowledgments

The authors wish to express their gratitude for the financial support received from Michelin and the Ecole Polytechnique. They thank J. Caillard, C. Astier and J. M. Clergeat, who obtained the experimental results presented in this paper. They also thank F. Lopez Jiménez for bringing references (Francis et al., 2006; Schultz et al., 2007; Lopez Jiménez and Pellegrino, 2012), to their attention.

References

Astier, C., Caillard, J., 2006. Etude de la flexion des renforts composites métalliques.
Bloch, F., 1928. Uber die quantenmechanik der elektronen in kristallgittern. Zeitschrift fur Physik A – Hadrons and Nuclei 52, 555–600.
Drapier, S., Grandidier, J.C., Potier-Ferry, M., 2001. A structural approach of plastic microbuckling in long fibre composites: comparison with theoretical and experimental results. International Journal of Solids and Structures 38, 3877–3904.
Francis, W.H., Lake, M.S., Schultz, M.R., Campbell, D., Dunn, M., Qi, H., 2006. Elastic memory composite microbuckling mechanics: closed-form model with empirical correlation. In: 48th AIAA/ASME/ASCE/AHS/ASC Structures, Structural Dynamics, and Materials Conference, Honolulu, HI.
Geymonat, G., Muller, S., Triantafyllidis, N., 1993. Homogenization of nonlinearly elastic-materials, microscopic bifurcation and macroscopic loss of rank-one convexity. Archive for Rational Mechanics and Analysis 122, 231–290.
Gong, L., Kyriakides, S., Triantafyllidis, N., 2005. On the stability of Kelvin cell foams under compressive loads. Journal of the Mechanics and Physics of Solids 53, 771–794.
Kyriakides, S., Arseculeratne, R., Perry, E.J., Liechti, K.M., 1995. On the compressive failure of fiber reinforced composites. International Journal of Solids and Structures 32, 689–738.
Le Tallec, P., Boussetta, R., Lignon, E., 2012. An enriched model of fiber reinforced thin flexible structures with in plane buckling capabilities. International Journal for Numerical Methods in Engineering 91, 872–895.
Lopez Jiménez, F., Pellegrino, S., 2012. Folding of fiber composites with a hyperelastic matrix. International Journal of Solids and Structures 49, 395–407.
Mathews, J.H., Fink, K., 2004. Numerical Methods using MATLAB, 4th ed. Prentice Hall.
Michailidis, P.A., Triantafyllidis, N., Shaw, J.A., Grummon, D.S., 2009. Superelasticity and stability of a shape memory alloy hexagonal honeycomb under in-plane compression. International Journal of Solids and Structures 46, 2724–2738.
Michel, J.C., LopezPamies, O., PonteCastaneda, P., Triantafyllidis, N., 2007. Microscopic and macroscopic instabilities in finitely strained porous elastomers. Journal of the Mechanics and Physics of Solids 55, 900–938.
Michel, J.C., LopezPamies, O., PonteCastaneda, P., Triantafyllidis, N., 2010. Microscopic and macroscopic instabilities in finitely strained fiber-reinforced elastomers. Journal of the Mechanics and Physics of Solids 58, 1776–1803.
Muller, S., 1987. Homogenization of nonconvex integral functionals and cellular elastic-materials. Archive for Rational Mechanics and Analysis 99, 189–212.
Nestorovic, M.D., Triantafyllidis, N., 2004. Onset of failure in finitely strained layered composites subjected to combined normal and shear loading. Journal of the Mechanics and Physics of Solids 52, 941–974.
Orjela, G., Riva, G., Fiorentini, F., 1998. The compression properties of tire reinforcement. Tire Science and Technology, TSTCA 26, 208–221.
Rosen, B.W., 1965. Mechanics of Composite Strengthening. American Society of Metals, Metals Park, OH, pp. 37–75.
Schaffers, W., 1977. Buckling in fiber-reinforced elastomers. Textile Research Journal 47, 502–512.
Schultz, M.R., Francis, W., Campbell, D., Lake, M.S., 2007. Analysis techniques for shape-memory composite structures. In: 47th AIAA/ASME/ASCE/AHS/ASC Structures, Structural Dynamics, and Materials Conference, Newport, RI.
Triantafyllidis, N., Maker, B.N., 1985. On the comparison between microscopic and macroscopic instability mechanisms in a class of fiber-reinforced composites. Journal of Applied Mechanics – Transactions of the ASME 52, 794–800.
Triantafyllidis, N., Nestorovic, M.D., Schraad, M.W., 2006. Failure surfaces for finitely strained two-phase periodic solids under general in-plane loading. Journal of Applied Mechanics – Transactions of the ASME 73, 505–515.
Triantafyllidis, N., Schraad, M.W., 1998. Onset of failure in aluminum honeycombs under general in-plane loading. Journal of the Mechanics and Physics of Solids 46, 1089–1124.
Vogler, T.J., Hsu, S.Y., Kyriakides, S., 2000. Composite failure under combined compression and shear. International Journal of Solids and Structures 37, 1765–1791.